Dynamic Three-Dimensional TLM Analysis of Microstriplines on Anisotropic Substrate

G. E. MARIKI AND C. YEH, FELLOW, IEEE

Abstract—**The frequency-dependent propagation characteristics of a hybrid mode along microstriplines on anisotropic substrates are presented for the case where the constitutive parameter tensors may be diagonalized. A generalization of the three-dimensional transmission-line-matrix (TLM) numerical procedure is used to obtain results for the phase constant β, effective permittivity ϵ_{eff}, and the characteristic impedance Z, all as functions of frequency and the shape ratio (w/h). Also shown are results for coupled microstrips on a sapphire substrate.**

I. Introduction

ALTHOUGH THE WORK reported in this paper was carried out several years ago (but unpublished) [1], recent interest in high-frequency (millimeter and submillimeter wave-length) microstrip circuits has prompted us to publish our results [2]. It appears that the transmission-line-matrix (TLM) approach that we used to solve the many problems dealing with enclosed microstrips with anisotropic and/or inhomogeneous substrates is rapidly becoming a very acceptable and viable way of dealing with these problems in spite of its demand for large computer memory and time [3], [4]. This is because of the enormous decrease in computational cost as well as the realization of the simplicity and versatility of the TLM approach as compared with other available numerical or analytical means [5]–[7].

Most of the original work on microstrip was based on a TEM approximation mainly because the resultant formulation is vastly simplified, and the solutions obtained agree closely with experimental results in the low-frequency range (below X-band). That this is so is exemplified by the pioneering works of Wheeler [8], using a conformal mapping technique, and Silvester [9] who applied a Green's function formulation. As the need arose for hybrid integrated circuits operating at frequencies as high as 20 GHz and above, the TEM solutions were no longer satisfactory since dispersion, which is significant at high frequencies, is ignored under a TEM approximation. Several techniques have been applied to determine the dispersion properties of microstrip. Among these were Getsinger's empirical formulation [10] and the TLM method used by Akhtarzad and Johns [11], [12]. The above-mentioned authors have presented results for the phase constant β and/or effective permittivity ϵ_{eff} as functions of frequency. Their results were strictly for isotropic substrates.

One of the practical design difficulties of using isotropic substrates, such as alumina, is the significant variation in the dielectric permittivity from different manufacturers or even from batch to batch from the same manufacturer. This essentially means that repeated measurements of the dielectric permittivity are required for accurate design of microstrip circuits. The use of anisotropic substrates with stable electrical properties, such as sapphire, alleviates this difficulty although it introduces a new problem in that new techniques have to be developed to analyze microstriplines on anisotropic substrates. The TEM approach was again used by Owens, Aitken, and Edwards [13] and Alexopoulos *et al.* [14] to determine the quasi-static properties of microstriplines on anisotropic substrates with a diagonal dielectric tensor $\underline{\underline{\epsilon}}$. Measurements of the dispersion characteristics of microstrip on sapphire substrates were also reported by Edwards and Owens [15]. The TEM solutions mentioned above suffer from the same limitations as those developed for isotropic substrates. The need for an efficient technique to determine the frequency-dependent (dynamic) propagation characteristics of microstriplines on anisotropic substrates is therefore apparent. This was the motivation behind our work which was completed in 1978. Since then a number of publications have appeared describing various techniques [5]–[7].

In the following, a description of the modified TLM technique applied to the enclosed microstrip on anisotropic substrate problems will be given. Numerical results with a discussion on the accuracy of the TLM technique will then be presented. Also shown are further examples showing the application to microstrip on periodically varying substrates as well as the coupled microstrips on anisotropic substrate.

II. The Transmission-Line-Matrix Technique

The geometry of the shielded microstripline is shown in Fig. 1. It consists of a conductive metallic strip of width w and zero thickness placed on a dielectric substrate of thickness h and a box-type enclosure of a perfectly conducting material. The thickness of the metallic strip is assumed to be vanishingly small and the properties of the

Manuscript received January 23, 1985; revised May 1, 1985.

The authors are with the Electrical Engineering Department, University of California at Los Angeles, Los Angeles, CA 90024.

0018-9480/85/0900-0789$01.00 ©1985 IEEE

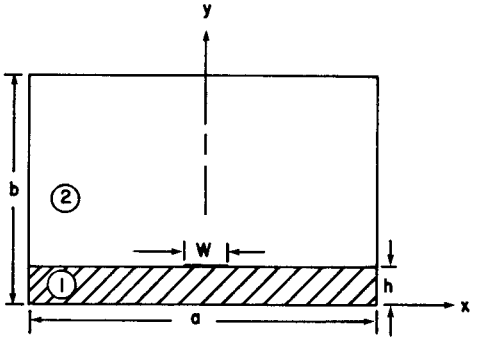

Fig. 1. Cross-sectional geometry of a single microstripline.

substrate are characterized by diagonal tensors of rank two, i.e., a dyadics, for the permittivity $\underline{\underline{\epsilon}}$, permeability $\underline{\underline{\mu}}$, and conductivity $\underline{\underline{\sigma}}$. The tensor elements are, in general, functions of the cross-sectional coordinates x and y in a rectangular coordinate system. Thus

$$\underline{\underline{\epsilon}} = \epsilon_0 \begin{bmatrix} \epsilon_{xx}(x,y) & 0 & 0 \\ 0 & \epsilon_{yy}(x,y) & 0 \\ 0 & 0 & \epsilon_{zz}(x,y) \end{bmatrix} \tag{1}$$

$$\underline{\underline{\mu}} = \mu_0 \begin{bmatrix} \mu_{xx}(x,y) & 0 & 0 \\ 0 & \mu_{yy}(x,y) & 0 \\ 0 & 0 & \mu_{zz}(x,y) \end{bmatrix} \tag{2}$$

$$\underline{\underline{\sigma}} = \begin{bmatrix} \sigma_{xx}(x,y) & 0 & 0 \\ 0 & \sigma_{yy}(x,y) & 0 \\ 0 & 0 & \sigma_{zz}(x,y) \end{bmatrix} \tag{3}$$

where ϵ_0 and μ_0 are the free-space permittivity and permeability, respectively. Maxwell equations in component form are

$$\frac{\partial E_z}{\partial y} - \frac{\partial E_y}{\partial z} = -\mu_0 \mu_{xx}(x,y) \frac{\partial H_x}{\partial t} \tag{4}$$

$$\frac{\partial E_x}{\partial z} - \frac{\partial E_z}{\partial x} = -\mu_0 \mu_{yy}(x,y) \frac{\partial H_y}{\partial t} \tag{5}$$

$$\frac{\partial E_y}{\partial x} - \frac{\partial E_x}{\partial y} = -\mu_0 \mu_{zz}(x,y) \frac{\partial H_z}{\partial t} \tag{6}$$

$$\frac{\partial H_z}{\partial y} - \frac{\partial H_y}{\partial z} = \left(\sigma_{xx}(x,y) + \epsilon_0 \epsilon_{xx}(x,y)\right) \frac{\partial}{\partial t} E_x \tag{7}$$

$$\frac{\partial H_x}{\partial z} - \frac{\partial H_z}{\partial x} = \left(\sigma_{yy}(x,y) + \epsilon_0 \epsilon_{yy}(x,y)\right) \frac{\partial}{\partial t} E_y \tag{8}$$

$$\frac{\partial H_y}{\partial x} - \frac{\partial H_x}{\partial y} = \left(\sigma_{zz}(x,y) + \epsilon_0 \epsilon_{zz}(x,y)\right) \frac{\partial}{\partial t} E_z. \tag{9}$$

The TLM technique will be used to solve the above set of equations together with the appropriate boundary conditions. We shall assume that the guided wave is propagating in the z-direction

$$E, H \sim e^{-j\beta z}$$

where β is the propagation constant.

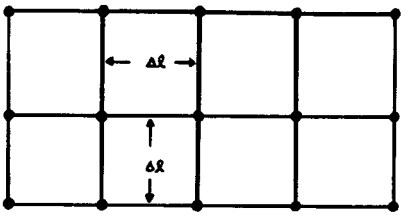

(a)

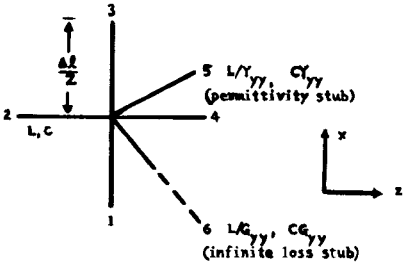

(b)

Fig. 2. (a) Shunt-connected TEM lines. (b) A generalized shunt node.

A. The Shunt Node

Fig. 2(a) shows how a number of ideal lossless two-wire transmission lines can be connected to form a two-dimensional transmission-line matrix. Shunt nodes are formed where the lines cross and these present impedance discontinuities for waves propagating along the lines. The internodal separation Δl is uniform throughout the matrix. Note that for clarity in Fig. 2(a), single lines are used to represent a transmission-line pair. A generalized shunt node is depicted in Fig. 2(b). Here an open-circuited shunt stub of length $\Delta l/2$ and normalized characteristic admittance Y_{yy} (normalized with respect to the characteristic impedance of the main line) is attached to the node. This is called the permittivity stub. Also shown in Fig. 2(b) is an infinite loss stub of normalized characteristic admittance G_{yy}. Hence, one notices that a pulse injected into the loss stub from the node will be completely lost. A lumped parameter equivalent network for an elementary matrix section is shown in Fig. 3. In this equivalent network, the short section of an open-circuited transmission line (the permittivity stub) is represented by a shunt admittance of value $(jY_{yy}/\sqrt{L/C})\tan(\omega \Delta l/2c)$. If $\omega \Delta l/2c = \pi \Delta l/\lambda \ll 1$, then $\tan(\omega \Delta l/2c) \simeq (\omega \Delta l/2)\sqrt{LC}$. Therefore, the admittance of the open-circuited stub is $\simeq j\omega C Y_{yy} \Delta l/2$. This can be recognized as a capacitive admittance. Hence, the total capacitance at the node is

$$C' = 2C\left(1 + \frac{Y_{yy}}{4} \Delta l\right). \tag{10}$$

The infinite loss stub of normalized characteristic admittance G_{yy} is represented by a lumped conductance of

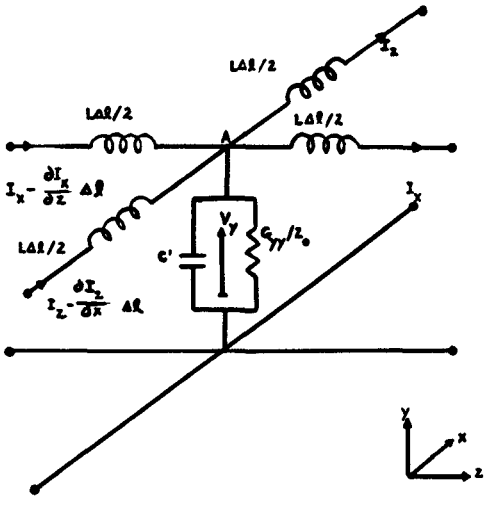

Fig. 3. Shunt node lumped network representation.

magnitude

$$G_{yy}\sqrt{\frac{C}{L}} = \frac{G_{yy}}{Z_0}$$

where

$$Z_0 = \sqrt{\frac{L}{C}}\,. \tag{11}$$

Application of Kirchoff's Current Law at node A gives (see Fig. 3)

$$\frac{\partial I_x}{\partial z} - \frac{\partial I_z}{\partial x} = \left[\frac{G_{yy}}{Z_0 \Delta l} + 2C\left(1 + \frac{Y_{yy}}{4}\right)\frac{\partial}{\partial t}\right] V_y. \tag{12}$$

The above analysis was carried out for a shunt node in the $x-z$ plane. A similar analysis for a shunt node in the $x-y$ and $y-z$ planes leads to, respectively,

$$\frac{\partial I_y}{\partial x} - \frac{\partial I_x}{\partial y} = \left(\frac{G_{zz}}{Z_0 \Delta l} + 2C\left(1 + \frac{Y_{zz}}{4}\right)\frac{\partial}{\partial t}\right) V_z \tag{13}$$

and

$$\frac{\partial I_z}{\partial_y} - \frac{\partial I_y}{\partial z} = \left(\frac{G_{xx}}{Z_0 \Delta l} + 2C\left(1 + \frac{Y_{xx}}{4}\right)\frac{\partial}{\partial t}\right) V_x. \tag{14}$$

One notes that the subscripts for the currents do not correspond to the coordinate direction along which the current flows; the subscripts are assigned at the series node (see Fig. 4) where a series node in, say, the $y-z$ plane has common node current I_x, etc. The choice of the subscripts makes it easier to identify the line equations with Maxwell's equations. The use of stubs, each with a different characteristic admittance, allows the TLM model to represent anisotropic media correctly.

From (7) and (14), the following equivalences between the TLM equation and Maxwell's equations can be identified:

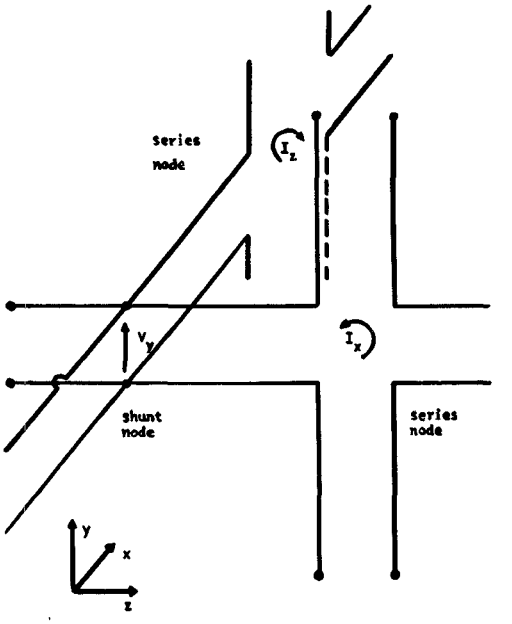

Fig. 4. A shunt node in the $x-z$ plane connected to series nodes in the $y-z$ and $x-y$ planes.

$$H_z \equiv I_z \tag{15}$$

$$H_y \equiv I_y \tag{16}$$

$$\sigma_{xx} \equiv \frac{G_{xx}}{Z_0 \Delta l} \tag{17}$$

$$\epsilon_0 \equiv 2C \tag{18}$$

$$\epsilon_{xx} \equiv \frac{4 + Y_{xx}}{4} \tag{19}$$

$$E_x \equiv V_x. \tag{20}$$

Similarly, from (8) and (12), we have

$$H_x \equiv I_x \tag{21}$$

$$E_y \equiv V_y \tag{22}$$

$$\sigma_{yy} \equiv \frac{G_{yy}}{Z_0 \Delta l} \tag{23}$$

$$\epsilon_{yy} \equiv \frac{4 + Y_{yy}}{4}. \tag{24}$$

Equations (9) and (13) yield the following equivalences:

$$E_z \equiv V_z \tag{25}$$

$$\sigma_{zz} \equiv \frac{G_{zz}}{Z_0 \Delta l} \tag{26}$$

$$\epsilon_{zz} \equiv \frac{4 + Y_{zz}}{4}. \tag{27}$$

From the above analysis, it is concluded that half of Maxwell's equations can be fully accounted for by three shunt nodes oriented in the $x-y$, $y-z$, and $x-z$ planes. The remaining half of Maxwell's equations will be satisfied by the series node.

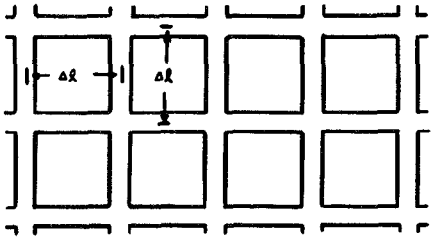

(a)

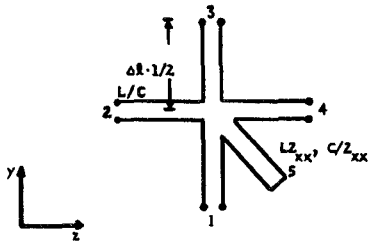

(b)

Fig. 5. (a) Series-connected TEM lines. (b) A generalized series node.

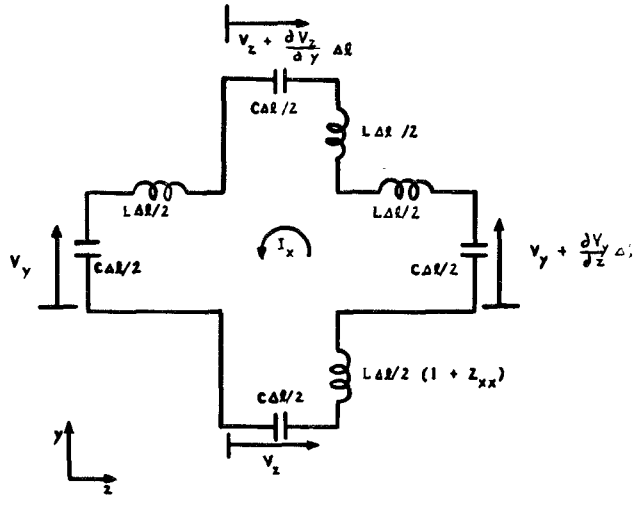

Fig. 6. Series node lumped network representation.

B. The Series Node

A series-connected two-dimensional transmission-line matrix is shown in Fig. 5(a). As in the shunt-connected TLM, the lines are ideal and lossless and the uniform mesh parameter is Δl. Fig. 5(b) shows a generalized series node which is equipped with a short-circuited stub called the permeability stub. The equations satisfied by the series node can be derived using the lumped parameter representation shown in Fig. 6. The input impedance of the short-circuited transmission line is

$$Z_{\text{in}} = jZ_{xx}\sqrt{\frac{L}{C}}\tan(\omega\Delta l/2c) \approx j\omega LZ_{xx}\Delta l/2. \quad (28)$$

The validity of (28) is the same as was stipulated for the short open-circuited stub associated with the shunt node, namely,

$$\frac{\omega\Delta l}{2c} = \frac{\pi\Delta l}{\lambda} \ll 1. \quad (29)$$

Equation (28) represents an inductive impedance, the magnitude of the inductance being

$$L' = \left(\frac{Z_{xx}}{2}\Delta l\right)L. \quad (30)$$

Application of Kirchoff's Voltage Law around the loop at the series node (Fig. 6) gives

$$\frac{\partial V_z}{\partial y} - \frac{\partial V_y}{\partial z} = 2L\left(1+\frac{Z_{xx}}{4}\right)\frac{\partial I_x}{\partial t}. \quad (31)$$

A series node in the $x-y$ and $x-z$ planes will, respectively, satisfy the following equations:

$$\frac{\partial V_y}{\partial x} - \frac{\partial V_x}{\partial y} = 2L\left(1+\frac{Z_{zz}}{4}\right)\frac{\partial I_z}{\partial t} \quad (32)$$

and

$$\frac{\partial V_x}{\partial z} - \frac{\partial V_z}{\partial x} = 2L\left(1+\frac{Z_{yy}}{4}\right)\frac{\partial I_y}{\partial t}. \quad (33)$$

The following additional equivalences complete the TLM modeling of Maxwell's equations:

$$\mu_0 \equiv 2L \quad (34)$$

$$\mu_{xx} \equiv \frac{4+Z_{xx}}{4} \quad (35)$$

$$\mu_{yy} \equiv \frac{4+Z_{yy}}{4} \quad (36)$$

$$\mu_{zz} \equiv \frac{4+Z_{zz}}{4}. \quad (37)$$

We have demonstrated that the use of three shunt and three series nodes oriented in the $x-y$, $x-z$, and $y-z$ planes enables all of Maxwell's equations for an inhomogeneous anisotropic medium to be accounted for properly. What remains is to devise a way of interconnecting the six nodes to form a three-dimensional node in space. One notices that no restriction on the spatial distribution or magnitudes of $\underline{\epsilon}$, $\underline{\mu}$, and $\underline{\sigma}$ has been placed.

C. The Three-Dimensional Node

Fig. 7 shows the construction of a three-dimensional node capable of representing three-dimensional space and satisfying Maxwell's equations for inhomogenous anisotropic media. The three-dimensional node is an interconnection of three shunt nodes and three series nodes structured in such a manner that there is one shunt node and one series node in each coordinate plane. The use of these six nodes results in a model that properly accounts for all of Maxwell's field equations. Again, in Fig. 7, a single line is used to represent a transmission-line pair. The nodes are named to correspond to the field quantity they represent.

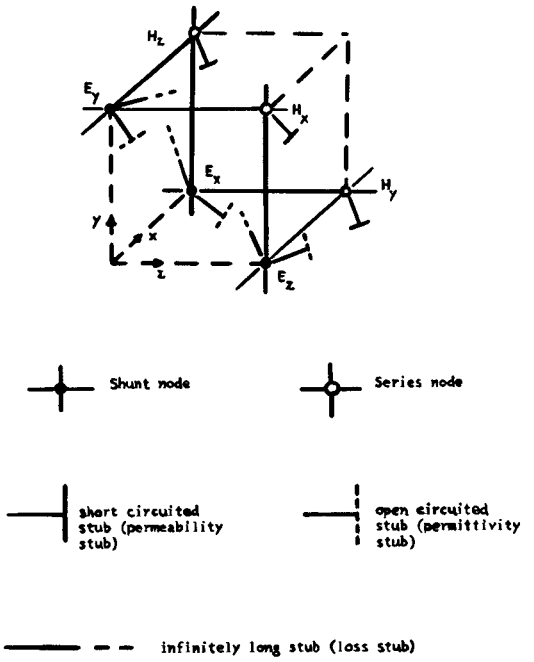

Fig. 7. A three-dimensional node.

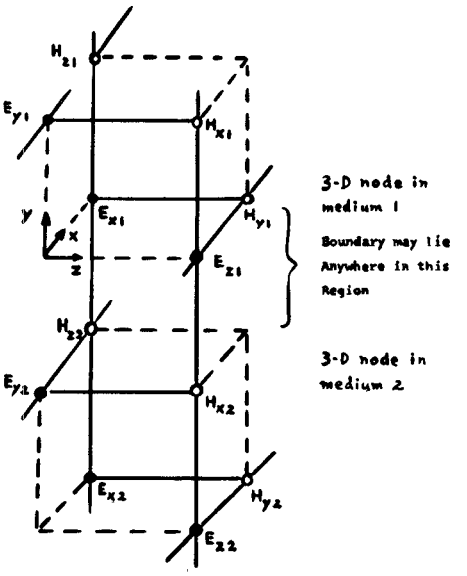

Fig. 8. Continuity of tangential fields across a dielectric boundary.

Thus, the common voltage at shunt node E_x corresponds to the x component of the electric field. The common current at series node H_x corresponds to the x component of the magnetic field, and so on.

To represent a three-dimensional propagation space, a number of these three-dimensional nodes are connected to form a three-dimensional mesh network. Maxwell's equations are thus satisfied at each three-dimensional node.

D. Boundary Conditions in the TLM Model

1) Electric and Magnetic Walls: In the plane of an electric wall, the tangential electric field must vanish. Similarly, in the plane of a magnetic wall, the tangential magnetic field must be zero. Since the corresponding quantities for the electric and magnetic field in the TLM model are the voltage and current in the transmission lines, electric and magnetic walls can be easily simulated in the TLM model by short-circuiting and open-circuiting the nodes, respectively. For example, to set E_x and E_y equal to zero in a particular plane, all shunt nodes E_x and E_y lying in that plane are shorted. To set, say, H_y and H_z equal to zero in some plane, the series nodes H_y and H_z in that plane are simply open-circuited.

2) Dielectric Boundary: The continuity of tangential electric and magnetic fields across a dielectric/dielectric boundary is automatically satisfied in the TLM model when the three-dimensional nodes are joined up by elementary sections of ideal transmission lines. For example, for a dielectric/dielectric boundary in the $x-z$ plane as shown in Fig. 8, since the common voltages at the shunt nodes correspond to the electric field and the common currents at the series nodes correspond to the magnetic field, the following equations valid for a transmission-line element joining the nodes on either side of the boundary are applicable:

$$E_{z1} = E_{z2} + \frac{\partial E_{z2}}{\partial y}\Delta l \tag{38}$$

$$E_{x1} = E_{x2} + \frac{\partial E_{x2}}{\partial y}\Delta l \tag{39}$$

$$H_{x1} = H_{x2} + \frac{\partial H_{x2}}{\partial y}\Delta l \tag{40}$$

$$H_{z2} = H_{z2} + \frac{\partial H_{z2}}{\partial y}\Delta l. \tag{41}$$

Since the voltage and current in the transmission line are smooth functions of position along the line, the continuity of the tangential fields across a boundary placed in between the nodes is assured.

E. The Numerical Procedure

1) Series and Shunt Nodes Scattering Matrices: In the TLM method, the numerical procedure involves determination of the impulse response of the network. Delta-function impulses are introduced at various locations in the matrix and these travel along the ideal transmission lines at the speed of light before being scattered at the nodes. Any of the six field components may be excited initially by specifying initial impulses at the appropriate nodes. Likewise, the response for any of the field components may be monitored by recording the pulses that pass through the relevant nodes.

The shunt and series nodes represent impedance discontinuities to the traveling pulses. From Figs. 2(b) and 3(b), the voltage scattering matrices for the shunt and series

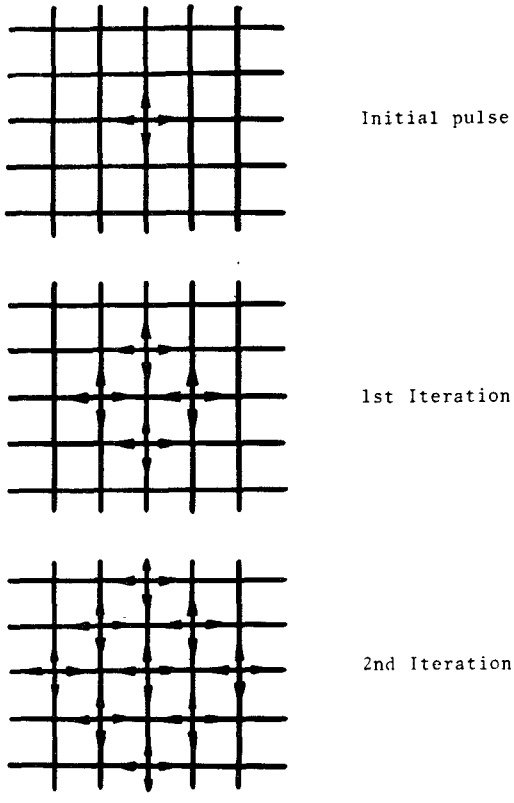

Fig. 9. Propagation of a point source on a two-dimensional homogeneous TLM model.

nodes are

$$[S]_{sh} = \frac{2}{Y}\begin{bmatrix} 1 & 1 & 1 & 1 & Y_{jj} \\ 1 & 1 & 1 & 1 & Y_{jj} \\ 1 & 1 & 1 & 1 & Y_{jj} \\ 1 & 1 & 1 & 1 & Y_{jj} \\ 1 & 1 & 1 & 1 & Y_{jj} \end{bmatrix} - [I] \tag{42}$$

where

$$Y = 4 + Y_{jj} + G_{jj} \tag{43}$$

$[I]$ is the unit matrix and *sh* stands for shunt. The subscripts *jj* may be *xx*, *yy*, or *zz* as appropriate. For the series node, we have

$$[S]_s = \frac{2}{Z}\begin{bmatrix} -1 & 1 & 1 & -1 & -1 \\ 1 & -1 & -1 & 1 & 1 \\ 1 & -1 & -1 & 1 & 1 \\ 1 & 1 & 1 & -1 & -1 \\ -Z_{jj} & Z_{jj} & Z_{jj} & -Z_{jj} & -Z_{jj} \end{bmatrix} + [I] \tag{44}$$

where

$$Z = 4 + Z_{jj}. \tag{45}$$

Thus, an impulse impinging on a shunt node would be scattered in accordance with (42) and an impulse incident on a series node would be scattered following (44).

2) Pulse Propagation in the TLM Model: The propagation of pulses in the TLM model is illustrated in Fig. 9, where the first two iterations following an initial excitation pulse in a two-dimensional shunt-connected transmission-line matrix are shown. For simplicity, we assume free-space propagation, in which case there are no open-circuited shunt stubs connected to the nodes. The distance between the nodes is Δl and the time interval between iterations is $t_0 = \Delta l/c$ since the individual pulses travel at the speed of light. Upon impinging on a node, the pulse is scattered into the four coordinate directions in accordance with (42).

Propagation in a three-dimensional model can be visualized in a similar manner. In this case, the pulses are scattered at the shunt nodes as well as the series nodes.

3) Form of Output and Accuracy of Results: The output response function consists of a train of impulses of varying magnitude in the time domain separated by a time interval $\Delta l/c$. Thus, the theoretical frequency response obtained by taking the Fourier transform of the output response consists of a series of delta functions in the frequency domain corresponding to the modal resonant frequencies of the cavity for which a solution exists. Truncation of the output impulse response function (due to practical reasons) causes a spreading of the solution delta function into $\sin x/x$ type curves.

Let $V_{\text{out}}(t)$ be the output impulse function taken for N iterations of the matrix, i.e., the function starts at time $t = 0$ and finishes at time $t = N\Delta l/c$. $V_{\text{out}}(t)$ may be regarded as an impulse function $V_\infty(t)$, extending to time = infinity multiplied by a rectangular time function $V_p(t)$ of unit height and width $N\Delta l/c$ as follows:

$$V_{\text{out}}(t) = V_\infty(t) \times V_p(t) \tag{46}$$

where

$$V_p(t) = \begin{cases} 1, & 0 \leqslant t \leqslant \dfrac{N\Delta l}{c} \\ 0, & \text{elsewhere} \end{cases}. \tag{47}$$

If the Fourier transform of $V_{\text{out}}(t)$, $V_\infty(t)$, and $V_p(t)$ are $S_{\text{out}}(f)$, $S_\infty(f)$, and $S_p(f)$, respectively, then the Fourier transform of (46) is given by the convolution of $S_\infty(f)$ and $S_p(f)$, i.e.,

$$S_{\text{out}}(f) = \int_{-\infty}^{\infty} S_\infty(\alpha) S_p(f - \alpha)\, d\alpha \tag{48}$$

and

$$S_p(f) = \frac{N\Delta l}{c} \frac{\sin \dfrac{\pi N \Delta l f}{c}}{\dfrac{\pi N \Delta l f}{c}} e^{-j(\pi N \Delta l f/c)}. \tag{49}$$

Equations (47) and (48) indicate that $S_p(f)$, a curve of $\sin x/c$ form, is placed in each of the positions of the delta functions of the exact response $S_\infty(f)$, in both the positive and negative frequency planes. The accuracy of the result depends on the number of iterations N, since the greater N, the sharper the maximum peak of the curve. The accuracy is also affected by interference from the tail regions of the reflected solutions in the negative frequency plane as well as from the tail regions of neighboring

solution points corresponding to other modes of propagation.

III. Accuracy of the TLM Approach

To study the accuracy of the TLM approach described above, we shall compare our results with those obtained using quasi-static approximations. Specifically, we shall consider the comparison of the single microstrip problem for which quasi-static solutions have been presented [13], [14]. The confidence we gain from this study will enable us to use this TLM technique to treat other microstrip problems and present results which have not been analyzed elsewhere.

Quasi-static solutions for the single microstrip problem have been computed by Owens *et al.* [13] and Alexopoulos *et al.* [14]. Owens *et al.* have applied the method of finite differences to compute the capacitance per unit length C. Knowing the value of C, they were able to compute the low-frequency effective dielectric constant ϵ_{e0}. An analytical expression for an equivalent isotropic dielectric constant ϵ_{req} was developed. The implication is that a microstripline on an isotropic substrate with a dielectric constant of ϵ_{req} would exhibit the same electrical behavior as a microstripline on sapphire. The expression given by Owens *et al.* is [13]

$$\epsilon_{req} = 12.0 - \frac{1.21}{1 + 0.39(\log(10w/h))^2}. \tag{50}$$

It must be emphasized that this equation is applicable to sapphire substrates only. Alexopoulos *et al.* approached the problem of a microstripline on an anisotropic substrate again from a quasi-static basis [14]. Their method is based on a Green's function formulation to compute the static capacitance of the line. Their results are presented in terms of the variation of the phase velocity with w/h.

Experimental measurements on the dispersion characteristics of microstrip on sapphire have been reported by Edwards and Owens [15]. In attempting to fit Getsinger's dispersion formula to their experimental results, they found an empirical formula for Getsinger's G factor for sapphire substrates.

The following scheme was adopted to verify the TLM solutions:

1) ϵ_{e0} and z_0 were determined from the TLM dispersion curves.
2) ϵ_{req} was computed from (50).
3) Getsinger's dispersion formula was used to determine ϵ_{eff} and this was compared with the TLM solutions.

Single crystal sapphire is a uniaxial crystal characterized by a dielectric tensor

$$\underline{\underline{\epsilon}} = \epsilon_0 \begin{bmatrix} \epsilon_{xx} & 0 & 0 \\ 0 & \epsilon_{yy} & 0 \\ 0 & 0 & \epsilon_{zz} \end{bmatrix} \tag{51}$$

with $\epsilon_{xx} = \epsilon_{zz} = 9.4$ and $\epsilon_{yy} = 11.6$. In writing (51), we have assumed that the crystal is oriented such that the y-axis is parallel to the optical axis. When used in microstrip circuits, sapphire substrates are usually cut with their plane surfaces perpendicular to the optical axis so that the material is constant everywhere in the plane of the substrate. A propagating wave along the microstripline is then not subjected to a change in permittivity at bends or corners in the line.

The geometry of the problem is shown in Fig. 1. The fundamental mode of propagation has even symmetry about the y-axis, i.e., at $x = 0$. Hence, the boundary conditions specified in the input data of the TLM computer program are:

1) $E_x = 0$ and $E_z = 0$ along $y = 0$ and $y = b$.
2) $E_y = 0$ and $E_z = 0$ along $x = a$.
3) $H_y = 0$ and $H_z = 0$ along $x = 0$.
4) $E_x = 0$ and $E_z = 0$ for $y = h$ and $-w/2 \leqslant x \leqslant w/2$.

The dielectric material was assumed to be lossless and so were the walls of the enclosure. Hence, to satisfy the above boundary conditions, infinite conductivity was specified along all electric walls, and even-mode symmetry about the y-axis was imposed thus making this axis a magnetic wall. Initially, the minimum number of nodes (corresponding to $h = \Delta l$) were used to obtain the dispersion curves for $w/h = 3, 5$. Dispersion analysis by the TLM technique involves resonating a section of the transmission line by placing shorting planes along the axis of propagation (the z-axis in this case), such that the images of the line in the shorting planes appear to be continuations of the structure. Each separation of the shorting planes then equals half of the guided wavelength for the fundamental mode at the frequency given by the resonant frequency of the cavity. If the distance between the shorting planes is $2L$, the phase constant is given by $\beta = \pi/2L$. For TEM waves, β is a linearly increasing function of frequency since the phase velocity is constant and uniform throughout the medium.

In Figs. 10 and 11, the TLM results for the dispersion curves depicting the phase constant as a function of frequency for $w/h = 3$ and $w/h = 5$ are shown. In both cases, the substrate height was $h = \Delta l$ and $b/h = 6$. Also shown in the same figures are the quasi-static solutions of Alexopoulos [14] and Getsinger's dynamic solutions computed as outlined above [10].

In executing the TLM program, 1000 iterations were used to ensure convergence of the solution. This figure on the number of iterations was arrived at after several runs of the entire program for iterations between 200 and 2000. Beyond 1000 iterations, the change in the resonant frequency of the cavity was less than 1.0 percent. For iterations less than 400, the TLM results were rather unstable, varying by as much as ± 10 percent from the convergent solution. This is because the peak of the $\sin x/x$ computer output response curve is not clearly defined for a low number of iterations (N). Also, the proximity of neighboring solution points corresponding to higher order even symmetry modes results in a larger error when N is small.

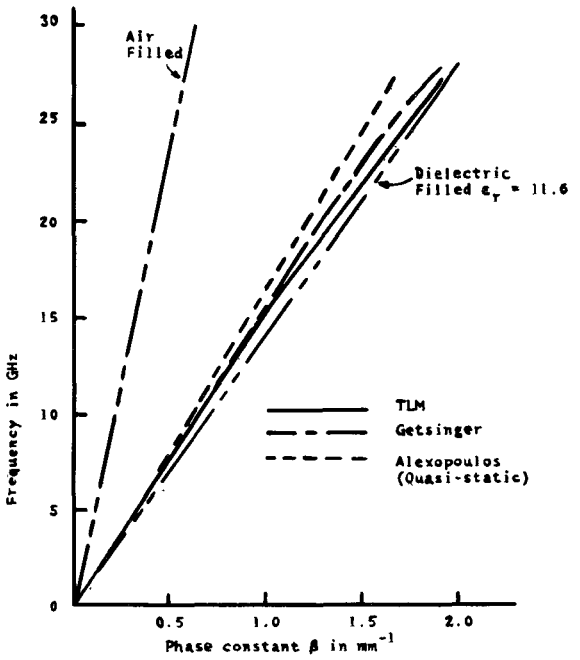

Fig. 10. Dispersion diagram for single microstrip on sapphire substrate $w/h = 3.0$, $h = \Delta l$.

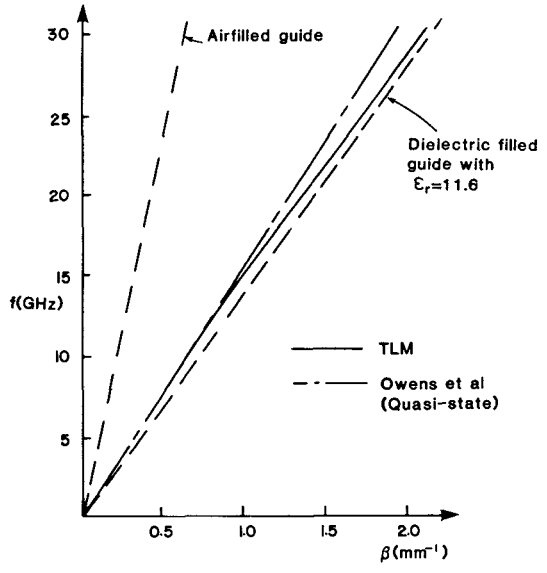

Fig. 11. Dispersion curves for the phase constant β ($w/h = 5.0$, $h = \Delta l$). Single microstrip on sapphire substrate.

To enhance the fundamental-mode field configuration, E_y was excited at all the nodes lying directly below the strip, and E_x was excited along the edge of the strip to provide the correct biasing for the field configuration of the fundamental mode. This choice was made again after a detailed study of the convergence of the results with respect to the manner in which the network was excited. Convergence was much faster if the approximate field distribution was specified at the onset and the network excited to enhance this mode. We note that the use of symmetry greatly reduces the storage requirements; this fact was fully exploited throughout the TLM analyses for the various problems treated in this paper.

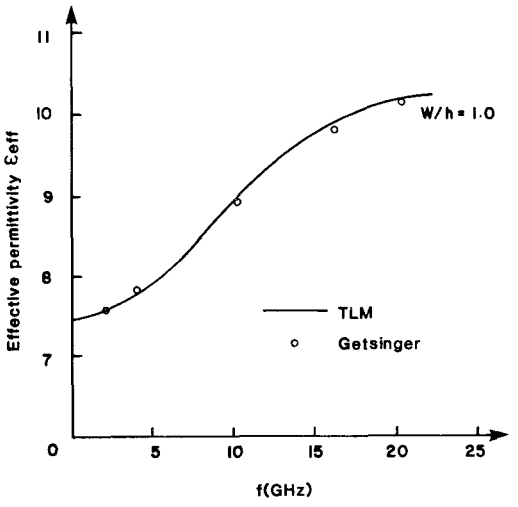

Fig. 12. Effective permittivity versus frequency ($w/h = 1.0$, $h = 3\Delta l$). Single microstrip on sapphire substrate.

Even though a very small number of nodes were used to describe the geometry of Fig. 1, the TLM solution was in very good agreement with Getsinger's dynamic solution (within 7 percent) and the low-frequency results agreed entirely with the quasi-static results due to Alexopoulos (see Figs. 10 and 11). Also shown in the same figures are the solutions for the air-filled and dielectric-filled microstrip.

Increasing the number of nodes should improve the accuracy of the TLM results. This was investigated by using two mesh points for the substrate, i.e., putting $h = 2\Delta l$. As before, E_y was excited at all nodes lying under the strip and E_x at all nodes along the edge of the strip. Agreement with Getsinger's result was improved from about 7 percent to better than 2 percent. The TLM results for this case are shown in Fig. 10 and 11. The quasi-static solutions obtained by Owens *et al.* using the method of finite differences are also shown for comparison at low frequencies [13]. Fig. 12 shows the variation of the effective permittivity with frequency for the case $w/h = 1$. Here, $h = 3\Delta l$ and agreement with Getsinger's result was extremely good—better than 0.5 percent for the most part.

A special feature of the TLM technique is the potential ability to determine the relative magnitudes of all the six electromagnetic-field components at a particular frequency for a specific mode of propagation, thus enabling a full hybrid-mode solution to be obtained with each run of the computer program. Defining the characteristic impedance of the microstripline as $Z_0 = E_y/H_x$ for a node lying directly below the center of the strip, we computed the frequency dependence of the characteristic impedance of the line.

The computation of the characteristic impedance was carried out simultaneously with the determination of the dispersion curves presented earlier, i.e., the voltage at the shunt node E_y and the current at series node H_x are recorded at the end of each iteration. The results are shown

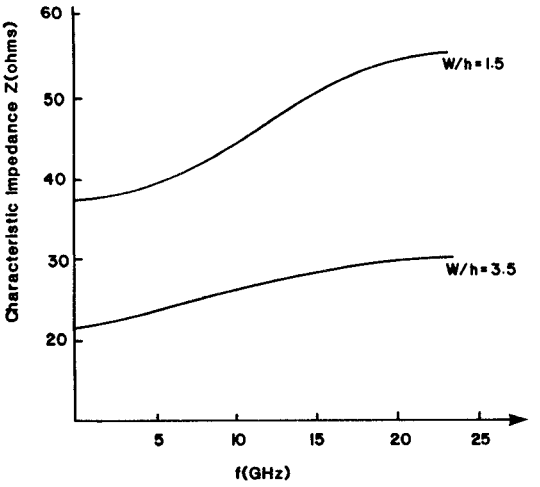

Fig. 13. Characteristic impedance versus frequency. Single microstrip on sapphire substrate with $h = 1.0$ mm.

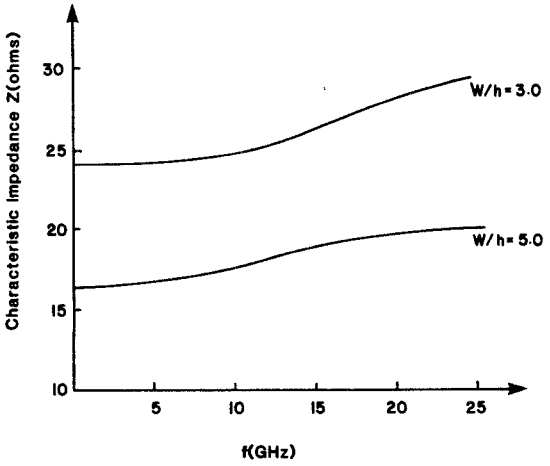

Fig. 14. Characteristic impedance versus frequency. Single microstrip on sapphire substrate with $h = 0.5$ mm.

in Figs. 13 and 14. The effective width of the microstrip line decreases with increasing frequency. Since the line impedance Z_0 is inversely proportional to the effective width w_{eff}, Z_0 therefore increases as frequency is increased.

As a further demonstration of the flexibility and generality of the TLM procedure, a gray-scale plot of the transverse field distribution was obtained for low and high frequencies. The nonhomogeneous field distribution is evident in Figs. 15 and 16, where E_y is plotted for single microstripline on sapphire with a strip-width to substrate-height ratio of 0.75. In order to see the details of the field distribution, more mesh points are needed than would be required in a dispersion analysis. In the above figures, four mesh points were used to describe the substrate, i.e., $h = 4\Delta l$, six mesh points were used for the free space above the strip. This was found to be adequate at a high frequency since most of the field was then concentrated in the substrate. At the lower frequency, the results were slightly modified by the upper wall of the enclosure, resulting in a flattening of the field distribution at the top. This effect was judged to be tolerable since the field intensity at the wall had decayed to about a tenth of its peak value.

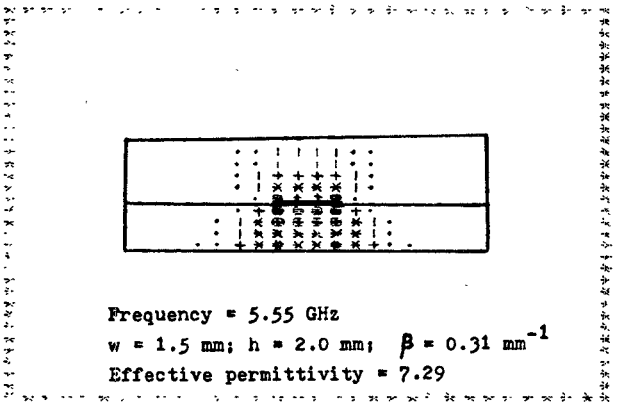

GREY-SCALE CHARACTERS AND RANGES

	0.00E+00	to	0.29E+02
•	0.29E+02	to	0.58E+02
-	0.58E+02	to	0.87E+02
+	0.87E+02	to	0.12E+03
*	0.12E+03	to	0.14E+03
#	0.14E+03	to	0.17E+03
%	0.17E+03	to	0.20E+03
@	0.20E+03	to	0.23E+03
@	0.23E+03	to	0.26E+03
@	0.26E+03	to	0.29E+03

Fig. 15. Electric-field (E_y) distribution for a single microstrip on sapphire substrate.

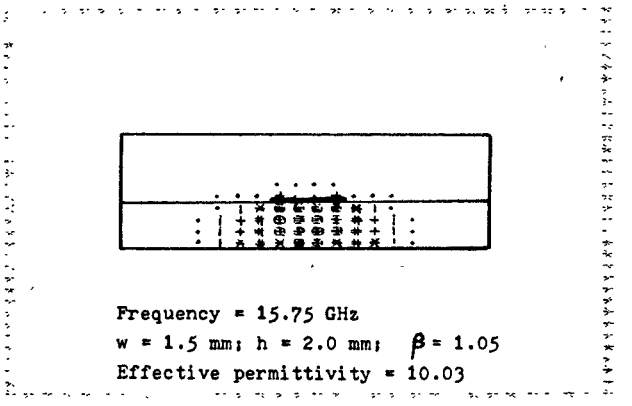

GREY SCALE CHARACTERS AND RANGES

	0.00E+00	to	0.26E+02
•	0.26E+02	to	0.53E+02
-	0.53E+02	to	0.79E+02
+	0.79E+02	to	0.11E+03
*	0.11E+03	to	0.13E+03
#	0.13E+03	to	0.16E+03
%	0.16E+03	to	0.18E+03
@	0.18E+03	to	0.21E+03
@	0.21E+03	to	0.24E+03
@	0.24E+03	to	0.26E+03

Fig. 16. Electric-field (E_y) distribution for a single microstrip on sapphire substrate.

IV. Numerical Examples

To demonstrate the versatility of the TLM method in solving different microstrip problems, we shall provide the following additional numerical examples.

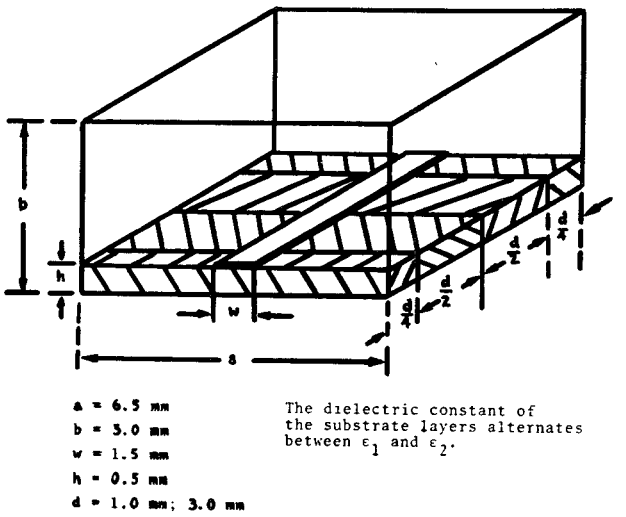

Fig. 17. Geometry of microstrip on substrate with periodically stratified index of refraction.

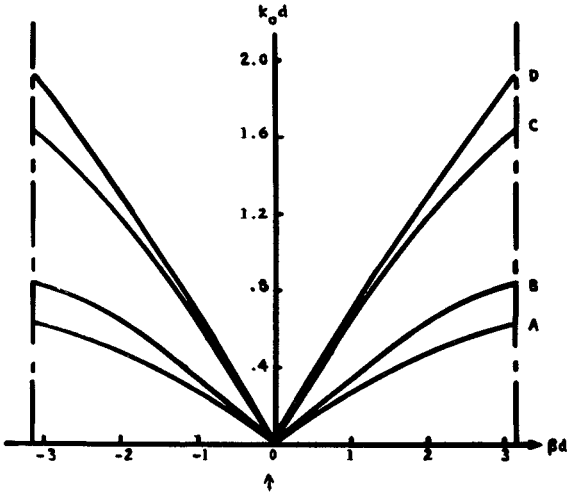

A. $\epsilon_1 = 10.0$, $\epsilon_2 = 20.0$; $d = 1.0$mm
B. $\epsilon_1 = 10.0$; $\epsilon_2 = 11.0$; $d = 1.0$mm
C. $\epsilon_1 = 2.00$; $\epsilon_2 = 3.00$; $d = 1.0$mm
D. $\epsilon_1 = 2.00$; $\epsilon_2 = 3.00$; $d = 3.0$mm

Fig. 18. $\omega - \beta$ diagram for microstrip on periodically stratified index of refraction.

A. Microstrip on Substrate with Periodically Stratified Dielectrics

Shown in Fig. 17 is a microstripline placed on a substrate made up of alternate layers of isotropic dielectric material of relative permittivities ϵ_1 and ϵ_2. The length of the period cell is d. Note that the two end layers in the cavity are of width $d/4$ so that the images of the structure in the end shorting planes appear to be continuations of the structure.

According to Floquet's theorem, an infinite set of spatial harmonics exists for guided waves along a periodic structure. These spatial harmonics must be present simultaneously in order that the total field may satisfy the boundary conditions. The eigenvalue equation for β for a periodic structure will always yield solutions $\beta_n = \beta + 2n\pi/d$, in addition to the fundamental solution. These other possible solutions are clearly the propagation constants of the spatial harmonics. A complete ω-β diagram thus exhibits k_0d as a periodic function of βd, that is, the βd curve is continued periodically outside the range

$$-\pi \leqslant \beta d \geqslant \pi.$$

The principal values of βd are plotted in Fig. 18 for various values of ϵ_1 and ϵ_2. The length of the unit cell in curves 1, 2, and 3 is $d = 1.0$ mm. The cutoff frequency for the low-frequency passband is given by the value of k_0d when $\beta d = \pm\pi$. Note that Fig. 18 shows only the first passband of the periodic structure. Examination of the diagram shows that the cutoff frequency may be reduced by increasing ϵ_1 or ϵ_2. Although the value of k_0d at cutoff was somewhat increased when the magnitude of d was tripled, the overall effect of increasing d was to reduce the cutoff frequency since k_0d did not triple at cutoff. In general, one may deduce the following conclusions: 1) To increase the upper cutoff frequency, one should lower the dielectric constant of the material. The phase velocity of the wave is lowered by reducing the length of the periodic cell. Hence, by controlling the width of the cell, it is possible to adjust the phase velocity of the wave. 2) Microstrip on a substrate with a periodically stratified index of refraction exhibits the slow-wave and filtering properties common to all periodic waveguiding structures.

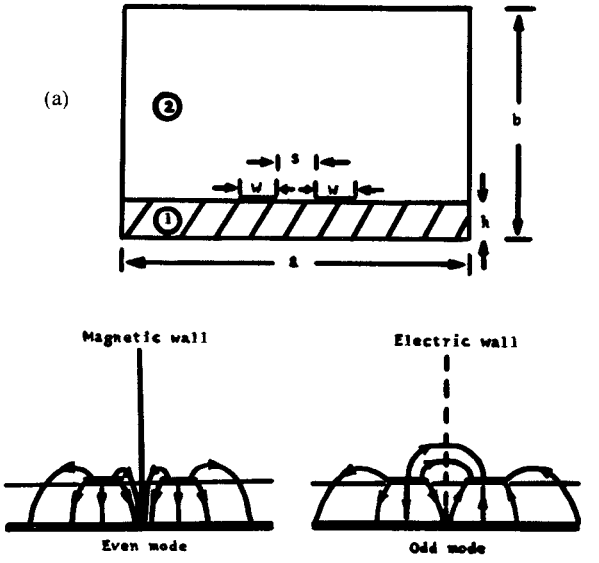

Fig. 19. (a) Cross-sectional geometry of coupled microstrip pair. (b) Electric flux lines for the two fundamental modes of two coupled microstrips.

B. Coupled microstriplines on Sapphire

The frequency-dependent even- and odd-mode phase constants were determined for the structure of Fig. 19

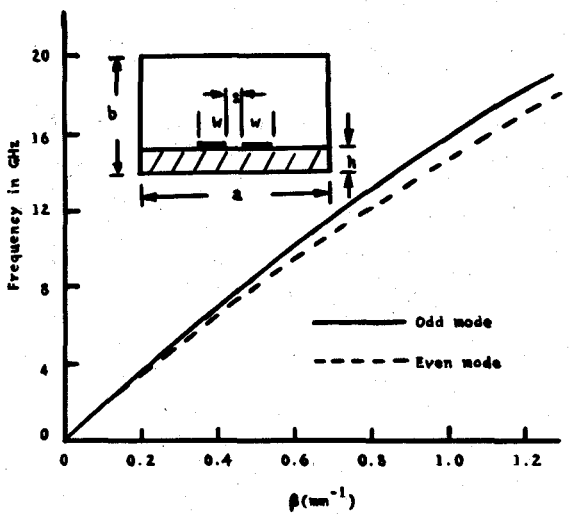

Fig. 20. Dispersion diagram for even and odd fundamental modes of edge-coupled microstrip.

using sapphire substrate as an example. Also computed was the frequency-dependent coupling length for the same structure. The results are depicted in Fig. 20. Although a b/h ratio of only 3 was used, the results obtained by moving the upper boundary farther away were not significantly different. The number of iterations of the computer program was kept at 1000 to minimize truncation errors.

V. Conclusions

The simplicity of the TLM technique in solving problems dealing with complex waveguiding structures should be noted. Although we have demonstrated only the solutions of microstrip problems, the technique can be easily extended to solve waveguiding problems for integrated optical circuits (IOC) or fiber optics [16]. The guiding medium may be anisotropic and inhomogeneous.

References

[1] G. E. Mariki, "Analysis of microstrip lines on inhomogeneous anisotropic substrates," Ph.D. dissertation, University of California, Los Angeles, June 1978.

[2] A. S. Kariotis, "The millimeter wave market: An overview," *Microwave J.*, vol. 27, no. 7, p. 24, 1984.

[3] D. Choi and W. J. K. Hoefer, "A scalar TLM model for three-dimensional wave simulation," *IEEE Trans. Microwave Theory Tech.*, 1984.

[4] T. Kitazawa and Y. Hayashi, "Propagation characteristics—strip lines with multi-layered anisotropic media," *IEEE Trans. Microwave Theory Tech.*, vol. MTT-31, pp. 429–433, 1983.

[5] A-M. A. El-Sherbiny, "Hybrid mode analysis of microstrip lines on anisotropic substrates," *IEEE Trans. Microwave Theory Tech.*, vol. MTT-29, p. 1261, 1981. N. Yoshida, I. Fukai, and J. Fuknoka, "Application of Bergeron's method to anisotropic media," *Trans. IECE Japan*, vol. J64B, pp. 1242–1249, 1981.

[6] H. Lee and V. K. Tripathi, "Spectral domain analysis of frequency dependent propagation characteristics of planar structures on uniaxial medium," *IEEE Trans. Microwave Theory Tech.*, vol. MTT-30, p. 1188, 1982. M. Horno, "Quasistatic characteristics of covered coupled microstrips on anisotropic substrates: Spectral and variational analysis," *IEEE Trans. Microwave Theory Tech.*, vol. MTT-30, p. 1888, 1982.

[7] R. Mittra and T. Itoh, "A new technique for the analysis of the dispersion characteristics of microstrip lines," *IEEE Trans. Microwave Theory Tech.*, vol. MTT-19, pp. 47–56, Jan. 1971. T. Itoh and R. Mittra, "Spectral domain approach for calculating the dispersion characteristics of microstrip lines," *IEEE Trans. Microwave Theory Tech.*, vol. MTT-21, pp. 496–499, July 1973.

[8] H. A. Wheeler, "Transmission-line properties of parallel strips separated by a dielectric sheet," *IEEE Trans. Microwave Theory Tech.*, vol. MTT-13, pp. 172–185, Mar. 1965.

[9] P. Silvester, "TEM wave properties of microstrip transmission lines," *Proc. Inst. Elec. Eng.*, vol. 115, pp. 43–48, Jan. 1968.

[10] W. J. Getsinger, "Microstrip dispersion model," *IEEE Trans. Microwave Theory Tech.*, vol. MTT-21, pp. 34–39, 1973.

[11] S. Akhtarzad and P. B. Johns, "The solution of Maxwell's equations in three space dimensions and time by the TLM method," *Proc. Inst. Elec. Eng.*, vol. 122, 1975.

[12] S. Akhtarzad and P. B. Johns, "Generalized elements for the TLM method of numerical analysis," *Proc. Inst. Elec. Eng.*, vol. 122, 1975.

[13] R. P. Owens *et al.*, "Quasi-static characteristics of microstrip on anisotropic sapphire substrates," *IEEE Trans. Microwave Theory Tech.*, vol. MTT-24, pp. 499–505, Aug. 1976.

[14] N. G. Alexopoulos, S. Kerner, and C. M. Krowne, "Dispersionless coupled microstrip over fused silica-like anisotropic substrates," *Electron. Lett.*, vol. 12, pp.579–580, Oct. 1976. N. G. Alexopoulos *et al.* "On the characteristics of single and coupled microstrip on anisotropic substrates," *IEEE Trans. Microwave Theory Tech.*, vol. MTT-26, June 1978.

[15] T. Edwards and R. P. Owens, "2–18 GHz dispersion measurements on 10–100 ohm microstrip lines on sapphire," *IEEE Trans. Microwave Theory Tech.*, vol. MTT-24, pp. 506–513, Aug. 1976.

[16] C. Yeh, K. Ha, and S. B. Dong, "Single mode optical waveguides," *Appl. Opt.*, vol. 18, p. 1490, 1979.

G. E. Mariki was born in Moshi, Tanzania, on December 1, 1948. He received the B.S. degree in electrical engineering from the University of London (Imperial College), England, in 1972, the M.S. degree in telecommunication systems from the University of Essex, England, in 1973, and the Ph.D. degree in electrical engineering from the University of California at Los Angeles (UCLA) in 1978.

From 1973–1975, he was a Lecturer in the Department of Electrical Engineering at the University of Dar es Salaam, Tanzania. From 1978–1980, he was an Assistant Professor of Electrical Engineering at the Carnegie-Mellon University, Pittsburgh. Dr. Mariki's present address is unknown.

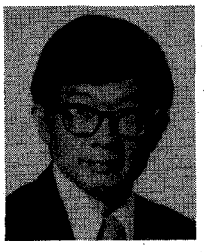

C. Yeh (S'56–M'63–SM'82–F'85) was born in Nanking, China, on August 11, 1936. He received the B.S., M.S., and Ph.D. degrees in electrical engineering from the California Institute of Technology, Pasadena, CA, in 1957, 1958, and 1962, respectively.

He is presently Professor of electrical engineering at the University of California at Los Angeles (UCLA). He joined UCLA in 1967 after serving on the faculty of USC from 1962 to 1967. His current areas of research interest are optical and millimeter-wave guiding structures, gigabit-rate fiber-optic local area network, and scattering of electromagnetic waves by penetrable irregularly shaped objects.

Dr. Yeh is a member of Eta Kappa Nu, Sigma Xi, and the Optical Society of America.